



Aerothermodynamic Study of a Generic EFP Configuration

Kirk J. Vanden
Douglas V. Nance

Air Force Research Laboratory, Munitions Directorate
AFRL/RWPC
101 West Eglin Boulevard
Eglin Air Force Base, FL 32542-6810

MAY 2010

CONFERENCE PAPER

This paper was presented at the 6th AIAA Biennial National Forum on Weapon System Effectiveness, 22 – 24 Sep 2009, at Raytheon Missile Systems, Tucson, CA, and is published in the conference proceedings. One of more of the authors is a U.S. Government employee working within the scope of his/her position. Should any party assert copyrights, the U.S. Government, as joint owner of this work, ahs for itself and others acting on its behalf, the right to copy, distribute, and use the work by or on behalf of the U.S. Government.

This paper is published in the interest of the scientific and technical information exchange.

Publication of this paper does not constitute approval or disapproval of the ideas or findings.

DISTRIBUTION A: Approved for public release; distribution unlimited. 96 ABW/PA Approval and Clearance # 96ABW-2009-0276, dated Sep 8 2009.

**AIR FORCE RESEARCH LABORATORY
MUNITIONS DIRECTORATE**

REPORT DOCUMENTATION PAGE				Form Approved OMB No. 0704-0188	
Public reporting burden for this collection of information is estimated to average 1 hour per response, including the time for reviewing instructions, searching existing data sources, gathering and maintaining the data needed, and completing and reviewing this collection of information. Send comments regarding this burden estimate or any other aspect of this collection of information, including suggestions for reducing this burden to Department of Defense, Washington Headquarters Services, Directorate for Information Operations and Reports (0704-0188), 1215 Jefferson Davis Highway, Suite 1204, Arlington, VA 22202-4302. Respondents should be aware that notwithstanding any other provision of law, no person shall be subject to any penalty for failing to comply with a collection of information if it does not display a currently valid OMB control number. PLEASE DO NOT RETURN YOUR FORM TO THE ABOVE ADDRESS.					
1. REPORT DATE (DD-MM-YYYY) 05-2010		2. REPORT TYPE Conference Paper		3. DATES COVERED (From - To)	
4. TITLE AND SUBTITLE Aerothermodynamic Study of a Generic EFP Configuration				5a. CONTRACT NUMBER	
				5b. GRANT NUMBER	
				5c. PROGRAM ELEMENT NUMBER 61102F	
6. AUTHOR(S) Kirk J. Vanden Douglas V. Nance				5d. PROJECT NUMBER 2307	
				5e. TASK NUMBER AM	
				5f. WORK UNIT NUMBER 60	
7. PERFORMING ORGANIZATION NAME(S) AND ADDRESS(ES) Air Force Research Laboratory, Munitions Directorate AFRL/RWPC 101 West Eglin Blvd Eglin AFB FL 32542-6810				8. PERFORMING ORGANIZATION REPORT NUMBER AFRL-RW-EG-TP-2010-7404	
9. SPONSORING / MONITORING AGENCY NAME(S) AND ADDRESS(ES) Same as Block 7				10. SPONSOR/MONITOR'S ACRONYM(S) AFRL/RW	
				11. SPONSOR/MONITOR'S REPORT NUMBER(S) AFRL-RW-EG-TP-2010-7404	
12. DISTRIBUTION / AVAILABILITY STATEMENT Distribution A. Approved for public release; distribution unlimited. 96 ABW/PA Approval and Clearance # 96ABW-2009-0276, dated Sep 8 2009.					
13. SUPPLEMENTARY NOTES SEE 'COVER PAGE' FOR PERTINENT METADATA INFORMATION.					
14. ABSTRACT The present study addresses the aerodynamics of a generic explosively formed penetrator body in Mach 6 hypersonic flight at sea level. As a first study of this type, the shape of the body is held fixed, and the flow field is resolved by applying state-of-the-art eddy simulation techniques in conjunction with a hybrid shock-turbulence capturing algorithm. Air is treated as a mixture of nitrogen and oxygen, and the governing equations are closed by a modern compressible turbulence closure term. Pressure is determined by using the thermally perfect gas equation of state applied to each species. The generic body also possesses an interior cavity. The flow field is captured both inside and outside of the body. Since aerodynamic breakup is of great concern, the distribution of temperature is determined on the body surfaces as well as temperature gradients based upon adiabatic wall boundary conditions. Also, the structure of the flow field is examined as is the time required for stationarity. These factors have an effect on flight stability.					
15. SUBJECT TERMS N/A					
16. SECURITY CLASSIFICATION OF:			17. LIMITATION OF ABSTRACT UU	18. NUMBER OF PAGES	19a. NAME OF RESPONSIBLE PERSON KIRK J. VANDEN
a. REPORT UNCLAS	b. ABSTRACT UNCLAS	c. THIS PAGE UNCLAS			19b. TELEPHONE NUMBER (include area code) 850-883-8658

Aerothermodynamic Study of a Generic EFP Configuration

Kirk J. Vanden^{*} and Douglas V. Nance[†]
Air Force Research Laboratory, Eglin AFB, FL, 32542-6810

The present study addresses the aerodynamics of a generic explosively formed penetrator body in Mach 6 hypersonic flight at sea level. As a first study of this type, the shape of the body is held fixed, and the flow field is resolved by applying state-of-the-art large eddy simulation techniques in conjunction with a hybrid shock-turbulence capturing algorithm. Air is treated as a mixture of nitrogen and oxygen, and the governing equations are closed by a modern compressible turbulence closure term. Pressure is determined by using the thermally perfect gas equation of state applied to each species. The generic body also possesses an interior cavity. The flow field is captured both inside and outside of the body. Since aerodynamic breakup is of great concern, the distribution of temperature is determined on the body surfaces as well as temperature gradients based upon adiabatic wall boundary conditions. Also, the structure of the flow field is examined as is the time required for stationarity. These factors have an effect on flight stability.

Nomenclature

e	=	specific internal energy
C_p	=	constant pressure specific heat
k^{sgs}	=	subgrid kinetic energy
E	=	total energy per unit mass
P	=	pressure
q_i	=	heat flux vector component
R_k	=	species k perfect gas constant
T	=	temperature
t	=	time
u_i	=	Cartesian velocity component
x_i	=	Cartesian coordinate
δ_{ij}	=	delta function
ρ	=	density
Δ	=	grid scale measure
τ_{ij}	=	stress tensor

I. Introduction

AN Explosively Formed Penetrator (EFP) is composed of two components, an explosive lens and a shaped metal liner as is shown in Figure 1.¹ As an EFP detonates, the detonation wave spreads through the lens. Controlled by the shape of the lens, the wave interacts and exerts a force distribution on the liner. The liner accelerates away from the blast, but the center region travels faster than the remainder of the liner. As a result, the liner takes on a crude bell-like shape. The distribution of explosive force causes the liner to undergo large, high strain-rate deformation. In flight, the liner drastically changes shape from a disk into a bell shaped bluff body. In some cases, an open cavity may exist at the base of the EFP. Structurally, the liner material “flows” in the plastic regime, and accordingly, it becomes very hot. The temperature rise due to the effects of material strain is complemented by aerodynamic heating from hypersonic flow in the thick atmosphere at sea level. It is of interest to investigate the

^{*} Technical Advisor, AFRL/RWAC, AIAA Associate Fellow.

[†] Research Scientist, AFRL/RWAC.

aerodynamics of a generic EFP body in the hypersonic regime, so we have chosen a sea level velocity corresponding to Mach 6 since this Mach number is comfortably within the hypersonic regime. In flight, the EFP may pitch or yaw in an unstable way; casting a complex pattern of aerodynamic loads over the EFP body. These forces can cause the EFP liner to break apart in flight. Investigating the phenomenon of aerostability and aerodynamic heating are focuses of the present study.

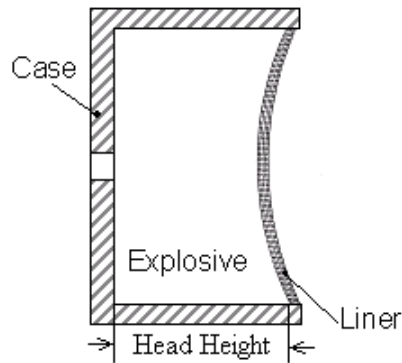


Figure 1. Cross-Section for a notional Explosively Formed Penetrator.

During the period of time encompassing the 1960s through the 1980s, hypersonic flow was intensively studied because of the design needs of reentry vehicles and concept designs such as the National Aerospace Plane.^{2,3} In deference to supersonic flow, there is no strict point of demarcation in terms of speed heralding the hypersonic regime. For aerospace vehicles commonly studied, the onset of hypersonic flow physics is encountered in the range of Mach 3 to Mach 5, or even higher. The physics associated with this

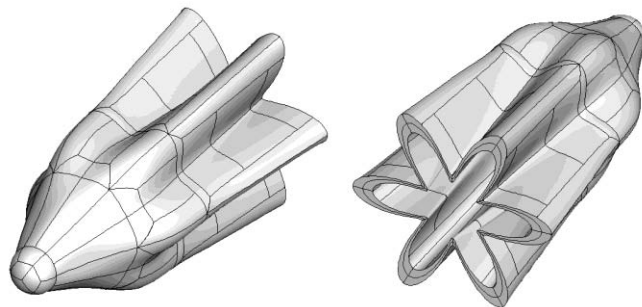


Figure 2. Geometric configuration for a generic EFP. Forward oblique view shown on the left, reverse oblique view shown on the right.

regime is very different that that associated with slower speed flow. Hypersonic flow is characterized by the presence of thin shock layers that lie between the body and the shock wave.² At higher Mach numbers, this layer becomes even thinner, and it may even merge with the boundary layer. The presence of an entropy layer is also characteristic of many hypersonic bluff body flow fields. Bluff (or blunted) bodies cause the formation of curved shock waves that stand some distance away from the body.

The strength of the shock wave and the attendant entropy jump changes along with shock curvature. It is strongest at the “nose” and weakens as the shock wave straightens downstream. This effect causes a flow with strong entropy and vorticity gradients to wash down the body thickening the boundary layer.² This phenomenon is important for an EFP since it spends much of its flight time as a bluff body and then can lengthen into a high aspect ratio body with a thin shock layer. The proximity of the shock wave along with its interaction with the boundary layer can dictate the forces and moments exerted on the body. These considerations have a significant effect on the stability of the EFP in flight.

High temperature gas dynamics are often encountered in hypersonic flow fields. In order to satisfy the no-slip boundary condition, the flow must reduce from hypersonic speed outside of the boundary layer to zero at the body surface. The mechanism decreasing the flow speed is viscous dissipation or friction. The kinetic energy of the flow is transformed into the internal energy of gas molecules in the boundary layer. As a result, boundary layer temperature increases dramatically.² In slower speed flow fields, this energy is absorbed mostly in molecular translational and rotational modes, but for hypersonic speeds, energy may be absorbed in vibrational modes. For sufficiently high speeds, gas molecules may either ionize or dissociate effectively resulting in a chemically reacting

flow field. The gas field can achieve very high temperatures, thousands of degrees Kelvin. This thermal energy is transferred in part to the EFP body softening the liner material and creating a major concern for weapon effectiveness.

The purpose of this study is to capture some of these effects for a realistic, yet constant, EFP geometry. Its velocity is held at constant Mach 6 for sea level flight conditions. It is in this sense that the EFP diverges from common hypersonic flow problems. Both re-entry and hypersonic flight occur in low density atmosphere. At sea level density, we have little aerodynamic data for this speed range.³ In the work that follows, the pitch angle is varied as a parameter over the range of zero to +7.5°. For each pitch angle, the time required to achieve a stationary flow field is determined. The existence of a stationary flow indicates that flow properties vary in a cyclical manner. That is to say, regions of recirculation may exist in the cavity resulting in cyclical pressure fluctuations on the body. As a result, the force and moment distributions alter on the EFP body. The flow field is unsteady but varies in a periodic manner. The settling time required to reach this state is also of theoretical interest. If the flow remains non-stationary for the duration of the flight, the body may continue to oscillate in pitch. This assertion is of added significance since our model EFP configuration has a fixed shape for the duration of the simulation. The temperature and temperature gradient distributions are also determined on the interior and exterior surfaces of the body. We also determine whether or not chemical reactions may occur in the flow field under these conditions. Trends in the fluctuation of force and moment are calculated at the different pitch angles.

II. Theory

The computer program Large Eddy Simulation with LInear Eddy modeling in 3 Dimension (LESLIE3D) has been used to generate the EFP flow field results shown later in the paper. LESLIE3D is developed by Suresh Menon at the Georgia Institute of Technology.⁴ This computer program has a core capability for dynamic large eddy simulation (LES). That is to say, flow field features existing at the scale of the grid or larger are simulated by numerical solution of the conservation equations. Flow features existing at the subgrid scales (scales smaller than the mesh size) must be modeled.⁵ The subgrid effects are represented in the conservation equations via closure terms.

A. Filtered Governing Equations

The conservation laws used for this research consist of the compressible Navier-Stokes equations cast in three dimensions. For real turbulent flow fields, we cannot solve these equations via direct numerical solution due to the limitations imposed by today's computer resources. Our LES approach first involves spatially filtering the governing equations at the grid scale in order to produce a set of turbulence closure terms that are later modeled. The filtered equations are written as follows.⁶

$$\frac{\partial \bar{\rho}}{\partial t} + \frac{\partial \bar{\rho} \tilde{u}_i}{\partial x_i} = 0 \quad (1)$$

$$\frac{\partial \bar{\rho} \tilde{u}_i}{\partial t} + \frac{\partial}{\partial x_j} [\bar{\rho} \tilde{u}_i \tilde{u}_j + \bar{P} \delta_{ij} - \bar{\tau}_{ij} + \tau_{ij}^{sgs}] = 0 \quad (2)$$

$$\frac{\partial \bar{\rho} \tilde{E}}{\partial t} + \frac{\partial}{\partial x_i} [(\bar{\rho} \tilde{E} + \bar{P}) \tilde{u}_i + \bar{q}_i - \tilde{u}_j \bar{\tau}_{ij} + H_i^{sgs} + \sigma_i^{sgs}] = 0 \quad (3)$$

$$\frac{\partial \bar{\rho} \tilde{Y}_k}{\partial t} + \frac{\partial}{\partial x_i} [\bar{\rho} \tilde{Y}_k (\tilde{u}_i + \tilde{V}_{i,k}) + Y_{i,k}^{sgs} + \theta_{i,k}^{sgs}] = \bar{\omega}_k \quad (4)$$

where $k = 1, \dots, N_s$, N_s being the number of gaseous chemical species involved in the calculation. Equations (1) through (4) are mass, momentum, energy and species conservation equations, respectively. Symbols $\bar{\rho}$, u_i , \bar{P} , Y_k and q_i are the mixture gas density, velocity component in Cartesian component direction x_i , absolute pressure, mass fraction for the k^{th} species and heat flux component in direction x_i , respectively. Symbol τ_{ij}

contains the components of the Cartesian shear stress tensor while E represents the total energy per unit volume, i.e.,

$$\tau_{ij} = \mu \left(\frac{\partial u_i}{\partial x_j} + \frac{\partial u_j}{\partial x_i} \right) + \lambda \frac{\partial u_l}{\partial x_l} \delta_{ij} \quad (5)$$

$$E = e + \frac{1}{2} u_l u_l \quad (6)$$

The summation convention is applied to the index l in (5) and (6). The Fickian diffusion velocities are given by $V_{i,k}$. The overbar \bar{A} notation indicates that the quantity A has been averaged without density weighting whereas the notation \tilde{A} indicates that A has been mass averaged. The subgrid stress tensor τ_{ij}^{sgs} , subgrid total enthalpy flux H_i^{sgs} , subgrid convective species flux Y_{ij}^{sgs} , subgrid viscous work σ_i^{sgs} and subgrid species diffusive work $\theta_{i,k}^{sgs}$ are turbulence closure terms that require modeling to some degree. Chemical reactions occurring between species are governed by the filtered reaction rate term $\bar{\omega}_k$.⁷ Pressure in the gas mixture is determined through the use of a filtered perfect gas equation of state, i.e.,

$$\bar{P} = \bar{\rho}(\tilde{R}\tilde{T} + T^{sgs}) \quad (7)$$

with R_U equal to the universal gas constant, and

$$\tilde{R} = \sum_{k=1}^{N_s} \tilde{Y}_k R_k = \sum_{k=1}^{N_s} \tilde{Y}_k \left(\frac{R_U}{MW_k} \right) \quad (8)$$

MW_k is the molecular weight of species k .⁸ The filtered mixture internal energy is given as

$$\tilde{e} = \sum_{k=1}^{N_s} \tilde{Y}_k e_{f,k}^0 + \sum_{k=1}^{N_s} \tilde{Y}_k \int_0^{\tilde{T}} C_{V,k}(T) dT + \sum_{k=1}^{N_s} E_k^{sgs} \quad (9)$$

In equation (9), $C_{V,k}$ is the constant volume specific heat for species k , and E_k^{sgs} is the subgrid internal energy for species k . The heat flux term may be written as⁷

$$\bar{q}_i = -\kappa \frac{\partial \tilde{T}}{\partial x_i} + \bar{\rho} \sum_{k=1}^{N_s} \tilde{h}_k \tilde{Y}_k \tilde{V}_{i,k} \quad (10)$$

where κ is the local coefficient of thermal conductivity, and⁸

$$\tilde{h}_k = \tilde{Y}_k h_{f,k}^0 + \tilde{Y}_k \int_0^{\tilde{T}} C_{P,k}(T) dT \quad (11)$$

The specific heat at constant pressure for species k is written as

$$C_{P,k} = C_{V,k} + R_k \quad (12)$$

B. Closure Term Modeling

Taken directly, the number of subgrid terms, denoted by superscript sgs , result in a system of governing equations that is not closed. In order to close this system of equations, the subgrid terms must be somehow modeled. The current practice is to neglect T^{sgs} , $\theta_{i,k}^{sgs}$ and E_k^{sgs} since these terms tend to be small.⁶ The crux of this modeling effort is in determining the subgrid stress tensor based upon the subgrid kinetic energy, i.e.,

$$\tau_{ij}^{sgs} = -2\nu_t \left(\tilde{S}_{ij} - \frac{1}{3} \tilde{S}_{kk} \delta_{ij} \right) + \frac{2}{3} k^{sgs} \delta_{ij} \quad (13)$$

where the evolution equation for subgrid kinetic energy is given by

$$\begin{aligned} \frac{\partial}{\partial t} (\bar{\rho} k^{sgs}) + \frac{\partial}{\partial x_i} (\bar{\rho} \tilde{u}_i k^{sgs}) &= \frac{\partial}{\partial x_i} \left[(\bar{\rho} \nu_t + \mu) \frac{\partial k^{sgs}}{\partial x_i} + \frac{\bar{\rho} \nu_t \tilde{R}}{\text{Pr}_t} \frac{\partial \tilde{T}}{\partial x_i} \right] \\ &\quad - \left(\overbrace{1 + \alpha_{pd} (M_t^{sgs})^2 \left(\frac{\bar{\rho} \tilde{S} k^{sgs}}{D_k^{sgs}} \right)^2}^* \right) \left(\tau_{ij}^{sgs} \frac{\partial \tilde{u}_j}{\partial x_i} + \bar{\rho} K_\epsilon \frac{(k^{sgs})^{3/2}}{\bar{\Delta}} \right) \end{aligned} \quad (14)$$

The subgrid kinetic energy is mathematically defined as

$$k^{sgs} = \frac{1}{2} (\widetilde{u_i u_i} - \tilde{u}_i \tilde{u}_i) \quad (15)$$

where the summation convention is in effect for the index i .⁹ Equation (12) is integrated along with the conservation equations, and since it is model equation, it relies on a set of parameters such as ν_t , the eddy viscosity, given by

$$\nu_t = K_\nu \sqrt{k^{sgs}} \bar{\Delta} \quad (16)$$

where K_ν is a coefficient set by the Locally Dynamic subgrid Kinetic energy Model (LDKM).^{8,10} The dissipation term for k^{sgs} is given by

$$D_{K^{sgs}} = \frac{\bar{\rho} K_\epsilon (k^{sgs})^{3/2}}{\bar{\Delta}} \quad (17)$$

with K_ϵ as the LDKM dissipation coefficient (analogous to K_ϵ); $\bar{\Delta}$ is the local grid scale measurement. Other parameters introduced in (12) are μ the dynamic viscosity, Pr_t the turbulent Prandtl number, M_t^{sgs} the turbulent Mach number based upon k^{sgs} , and α_{pd} is a pressure-dilatational scaling coefficient. Note also that (13) and (14) are tightly coupled through the presence of both k^{sgs} and τ_{ij}^{sgs} .

The theory that underlies LDKM is quite complex, and the details of implementing the above equations (along with others not shown) are beyond the scope of this paper. However, it is worthwhile to discuss the physical meaning behind this model. In the first place, one may note the number of coefficients existing in (11), (12), (14) and (15). The proliferation of coefficients indicates that LDKM is indeed a model, but these coefficients are not tunable. Instead, they are in most cases based upon knowledge of the dynamic behavior of turbulent compressible flow fields. That is to say, these coefficients are set either autonomously by LDKM operating in dynamic mode, or they have fixed or easily calculated values.¹⁰ Also, LDKM diverges from most contemporary dynamic LES models through the presence of the term marked by an (*) asterisk. This term represents dilatational effects within the flow field due to pressure. It is through this term that (14) truly becomes representative of highly compressible flow fields, so this equation stands as a hallmark for state-of-the-art research in this field. When operating LDKM in dynamic mode, the subgrid scale properties are made to behave in an inertially correct manner with respect to the resolved flow field.

III. Numerical Methods

In the preceding section, the Navier-Stokes equations are presented along with the equations for Menon's LDKM. These equations are well suited for describing turbulent flow fields in any flight regime (subsonic, supersonic and hypersonic). In this section, we discuss the numerical algorithms associated with solving these equations. The EFP problem requires hypersonic flow solutions characterized by the presence of strong shock waves and high temperature gas dynamics. It is difficult for computer codes to at the same time capture both shock waves and subtle turbulent flow field fluctuations because each of these phenomena requires the use of different numerical algorithms. Generally, numerical dissipation must be used to dampen oscillations around shock waves, yet this same dissipation washed away the weaker vortical motions associated with turbulence. Moreover, high order centered difference stencils are usually required to accurately capture turbulence, but these stencils cause severe spurious oscillations around shock waves. It is also important to realize that the shock-capturing algorithms must be able to contend with complex equations of state. You may recall that we must apply the thermally perfect gas equation of state in the hypersonic flight regime. After performing several years of research, we have arrived at a numerical scheme that is eclectically composed of two parts. For shock-capturing, we apply what is referred to as the Harten-Lax-van Leer-Contact/Einfeldt (HLLC/E) approximate Riemann solver.^{11,12} In smooth regions of the flow field, we apply a second/fourth order MacCormack solver used in the earlier incarnations of LESLIE3D. A switching algorithm allows the computer program to autonomously select the appropriate space scheme based upon local properties throughout the flow field. Below, we present brief descriptions of the spatial integration schemes.

A. The HLLC/E Approximate Riemann Solver

HLLC/E is composed of HLL (HLL-Einfeldt), a scheme that does not preserve the contact wave, and HLLC (HLL-Contact), a scheme that does capture the contact wave. In this context, the contact wave is, in fact, a contact discontinuity, a common flow feature exhibited by the shock tube problem as well as by strong blast waves. These Godunov-like schemes are constructed on a one-dimensional coordinate oriented normal to a finite volume interface. It is in this manner that these schemes are applicable to three-dimensional flow fields. The numerical solution is calculated for a vector of conserved variables

$$\vec{U} = (\rho, u, v, w, \rho E, \rho k^{sgs}, \rho Y_1, \dots, \rho Y_{N_s}) \quad (18)$$

the associated flux vector

$$\vec{F} = (\rho q, \rho u q + P n_x, \rho v q + P n_y, \rho w q + P n_z, (\rho E + P) q, \rho k^{sgs} q, \rho Y_1 q, \dots, \rho Y_{N_s} q) \quad (19)$$

where $q = u n_x + v n_y + w n_z$, and $\hat{n} = n_x \hat{i} + n_y \hat{j} + n_z \hat{k}$ is the unit surface normal vector at the interface. Based upon these definitions, the HLLC numerical flux vector can be written as¹³

$$\vec{F}_{i+1/2}^{HLLC} = \begin{cases} \vec{F}^L, & 0 \leq S^L \\ \vec{F}^*, & S^L \leq 0 \leq S^R \\ \vec{F}^R, & S^R \leq 0 \end{cases} \quad (20)$$

where

$$\vec{F}^* = \frac{S^R \vec{F}^L - S^L \vec{F}^R + S^L S^R (\vec{U}^R - \vec{U}^L)}{S^R - S^L} \quad (21)$$

The Einfeldt wave speed estimates are

$$S^L = \min(q^L - c^L, \tilde{q} - \tilde{c}); \quad S^R = \max(q^R + c^R, \tilde{q} + \tilde{c}) \quad (22)$$

In (22), c is the speed of sound, and the notation $(\tilde{\cdot})$ indicates the Roe average.¹⁴ This numerical flux works quite well for hypersonic flow and is not susceptible to contact instabilities that can occur when strong bow shocks are aligned with the grid. Unfortunately, because of dissipative effects near the contact wave, it cannot be used for

extended regions of turbulent flow.¹³ In turbulent regions of the flow field, the HLLC numerical flux shows improved performance. The numerical flux for the HLLC scheme has a different form, i.e.,

$$\vec{F}_{i+1/2}^{HLLC} = \begin{cases} \vec{F}^L & , \quad 0 \leq S^L \\ \vec{F}^{L*} = \vec{F}^L + S^L(\vec{U}^{L*} - \vec{U}^L), & S^L \leq 0 \leq S^* \\ \vec{F}^{R*} = \vec{F}^R + S^R(\vec{U}^{R*} - \vec{U}^R), & S^{L*} \leq 0 \leq S^R \\ \vec{F}^R & , \quad S^R \leq 0 \end{cases} \quad (23)$$

In (23), intermediate states \vec{U}^{L*} and \vec{U}^{R*} have been introduced in order to model the presence of the contact discontinuity. These states may be written as¹³

$$\vec{U}^{L*} = \alpha^L \vec{U}^L + (0, \rho^L \omega^L n_x, \rho^L \omega^L n_y, \rho^L \omega^L n_z, \psi^L, 0, \dots) \quad (24)$$

with

$$\beta^L = \frac{S^* - q^L}{S^L - S^*}; \quad \alpha^L = \beta^L + 1; \quad \omega^L = -\beta^L(q^L - S^L) \quad (25)$$

and the intermediate wave speed

$$S^* = \frac{P^R - P^L + \rho^L q^L (S^L - q^L) - \rho^R q^R (S^R - q^R)}{\rho^L (S^L - q^L) - \rho^R (S^R - q^R)} \quad (26)$$

The state \vec{U}^{R*} is formed by replacing R for L in (24) through (26). In LESLIE3D, both of these numerical flux formulations are used to form the HLLC/E scheme. We state the result only, i.e.,

$$\vec{F}_{i+1/2}^{HLLC/E} = \begin{cases} \vec{F}_{i+1/2}^{HLLC}, & (d_{p,j} < 0 \text{ and } d_{u,j} < 0) \text{ or } (d_{p,k} < 0 \text{ and } d_{u,k} < 0) \\ \vec{F}_{i+1/2}^{HLLC}, & \text{otherwise} \end{cases} \quad (27)$$

This method requires shock detection in directions transverse to the direction of the interface normal, so

$$d_{p,j} = \frac{|P_{i,j+1,k} - P_{i,j-1,k}|}{\min(P_{i,j+1,k}, P_{i,j-1,k})} - \frac{1}{3} \quad (28)$$

$$d_{u,j} = u_{i,j+1,k} - u_{i,j-1,k} \quad (29)$$

and so forth.

A close inspection of the numerical flux formulas above reveals that the computation of the numerical flux first requires the left (L) and right (R) states be identified at interface location ($i + 1/2$). These “upwind” states are reconstructed from the data stored in the finite volume cells. This process is accomplished with the use of Monotone Upwind Scheme for Conservation Laws (MUSCL) interpolation.¹⁴ High order interpolation also requires the use of a nonlinear limiter with “flattening”¹⁵ in order to maintain data monotonicity.¹³ The details of these procedures are omitted from this work; interested readers are initially referred to References 13 through 15.

B. The MacCormack Solver

For the “hybrid” solver, that is suitable for capturing shock waves and turbulence anywhere in the flow field, it is necessary to switch between the upwind scheme and a centralized scheme based upon MacCormack’s method when calculating the numerical flux at interfaces. The finite difference version of this scheme uses forward and backward differences alternatively to remove bias from numerical error. For the finite volume scheme, we choose forward and backward upwind variables alternatively for the flux computation, i.e.,

$$\vec{F}_{i+1/2}^{Num} = \vec{F}(\vec{U}_{i+1/2}^{\pm}) \quad (30)$$

where

$$\vec{U}_{i+1/2}^+ = \vec{U}_{i+1}; \quad \vec{U}_{i+1/2}^- = \vec{U}_i \quad (31)$$

It can be shown that this scheme is stable and second order accurate in space.¹³ LESLIE3D also offers a MacCormack scheme accurate to the fourth order. The hybrid method is required to switch back and forth between the upwind and MacCormack solvers. The “switch” is based upon the “smoothness” of the flow field.⁸ Principally, LESLIE3D autonomously switches on the upwind scheme only in the vicinity of flow field discontinuities and employs the MacCormack solver in smooth regions of the flow field. This hybrid methodology performs quite well and has been extensively validated for the Richtmyer-Meshkov instability, the chosen test problem for this research.⁹ It has shown a great deal of efficacy for simulating shock-turbulence interaction problems.⁷

C. Time Integration Scheme and Computer Code Structure

LESLIE3D utilizes explicit time integration to capture the physics associated with unsteady flow fields. Although, the explicit time step is limited by the Courant-Friedrich-Lewy (CFL) criteria, it presents a high level of efficiency and computational simplicity on parallel machines. A version of the modified Euler method is applied for the MacCormack, upwind and hybrid schemes. This time integration method (in two steps) is succinctly summarized for one space dimension as follows.¹⁶

$$\vec{U}_i^* = \vec{U}_i^{n-1} + \frac{\Delta t}{\Delta x} (\vec{F}_{i+1/2}^{Num,n-1} - \vec{F}_{i-1/2}^{Num,n-1}) \quad (32)$$

$$\vec{U}_i^n = \frac{1}{2} \left[\vec{U}_i^* + \vec{U}_i^{n-1} - \frac{\Delta t}{\Delta x} (\vec{F}_{i+1/2}^{Num,*} - \vec{F}_{i-1/2}^{Num,*}) \right] \quad (33)$$

Equations (32) and (33) require minor adaptations for use with problems cast in three dimensions. Basically, the length term Δx roughly corresponds to a ratio of the cell volume to an average surface area for the interface normal to the coordinate indexed by i . The advective terms in (1) through (4) are easily discretized for structured, hexahedral finite volumes while the viscous terms require a basic generalized coordinate transformation. The mathematical procedures are relatively easy to accomplish and are quite robust.

It is prudent to discuss the larger aspects of LESLIE3D as well. LESLIE3D is a finite volume solver written for arbitrary structured grids and is fully parallelized. The current version of the code is implemented in multi-block form for analyzing highly complex flow configurations. LESLIE3D is also equipped with finite rate chemistry algorithms with a choice of turbulent chemical closure schemes. For problems involving evaporating reactive droplets or solid particles, LESLIE3D offers a dispersed phase that is fully coupled with the gas phase. A dense dispersed phase algorithm has recently been implemented within the computer program lending to its capability for solving multiphase physics problems.

IV. TEST PROBLEMS AND RESULTS

A. Problem Set-up and Basic Aerostability Analyses

A hypersonic flow field consisting of nitrogen and oxygen surrounding the generic EFP configuration (shown in Figure 2) has been analyzed. In this example, the EFP travels at Mach 6 under normal atmospheric conditions at sea level. Four pitch angles have been analyzed for this study: 0° , 2.5° , 5° and 7.5° . Other flight attitudes are certainly possible (including yaw angles), but the constraints of computer availability have only permitted the time required to consider these four conditions. The lobed design of the EFP complicates the flow field geometry. In addition to the exterior region, the flow field is also computed inside of the EFP folds; see Figure 2. The EFP body is non-deforming, and the pitch angle far field conditions are implemented along the outer boundary of the grid. Since the freestream is supersonic, the enforcement of these conditions presents no difficulty for the range of pitch angles under consideration. The grid is broken into 243 subdomains and consists of just over 4.6 million grid points. For efficient parallel computing, the subdomains are balanced to operate on 144 processors. For each pitch case, the flow field is “impulsively” started by initializing the flow in each cell to a velocity of 100 m/s in the direction of the freestream. As LESLIE3D operates, the flow field then stabilizes to a stationary solution around the EFB body permitting the collection of physical information including the temperature distribution on the body.

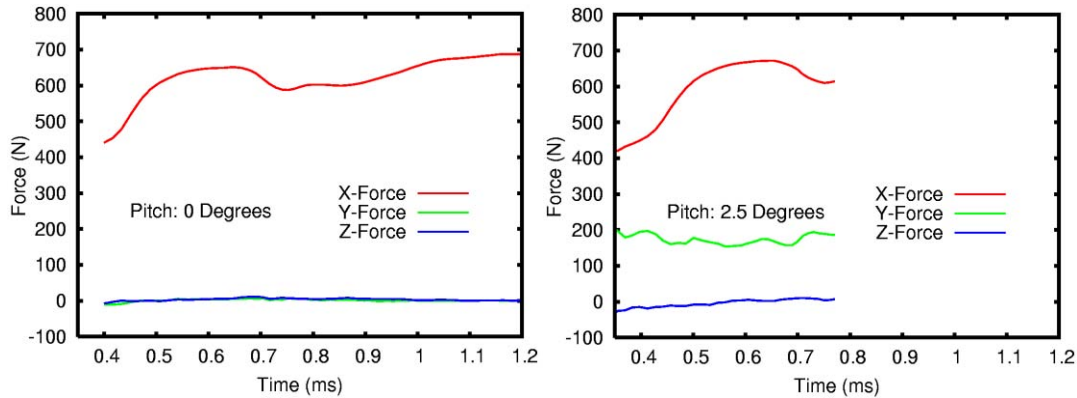


Figure 3. Components of total force in Newtons exerted on the EFP at (left) 0° pitch and (right) 2.5° pitch.

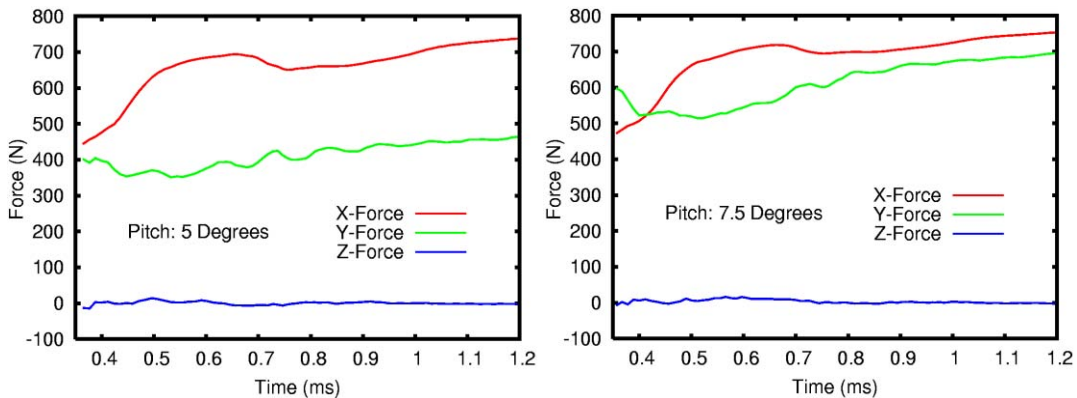


Figure 4. Components of total force in Newtons exerted on the EFP at (left) 5° pitch and (right) 7.5° pitch.

The settling time for the flow field is of great interest since time is required for the flow field to stabilize around a real EFP that has just been fired. Figure 3 contains plots of the total force components exerted on the EFP in the x for pitch angles 0° and 2.5° , respectively. Figure 4 contains corresponding plots for the 5° and 7.5° pitch cases. As one can see, for the 5° and 7.5° cases (Figure 4), the flow field does not begin to exhibit stationarity until over 1 ms of flight time has elapsed. The same trend is exhibited in Figure 3, but as this manuscript is being drafted, the numerical solutions are still in progress for the 0° and 2.5° pitch angles. At Mach 6, the elapsed flight time of one millisecond corresponds to about 28 body lengths or 2.25 meters of travel. For earlier times, the flow field around the body is expected to be highly unsteady, but non-inertial calculations are needed to prove this assertion. In Figure 5, total force exerted in the x direction is shown for each of the pitch cases. For the 7.5° case, the force exceeds that exhibited at 5° pitch due to the increased angle of attack, i.e., more of the body's surface area is exposed to increased pressure drag. It is expected that this trend will also be reflected in the 0° and 2.5° pitch cases. However, due to the restrictions of time, the computer solution for the 2.5° case has not yet advanced far enough to prove this assertion. Still, from the trend observed thus far, it seems unlikely that a conventional EFP will achieve stationary flow conditions within its normal time of flight. If this assertion bears true, it may have interesting implications for aerostability. The inherent unsteadiness of the flow field may complicate the process of stabilizing the EFP's flight. We can also differentiate between the effects of pressure and viscous forces. The generic EFP geometry is still a streamlined body, so it is expected that the force due to pressure exceeds that of skin friction drag. Generally, we do not speak of "lift" for this type of body, but both drag and significant side forces do arise. (See Figures 3 and 4). This assertion is illustrated by Figure 6, a plot comparing total force with skin friction drag (or viscous force) for pitch angles 0° , 2.5° , 5° and 7.5° . From this graph, we can conclude that the forces exerted by pressure (including the shock wave drag) overwhelm viscous forces exerted on the EFP. The total force magnitude increases along with the pitch angle. Interestingly, the viscous force retains essentially the same magnitude in time as the pitch angles changes. It follows that the fluctuating pressure force dominates the motion of the EFP, at least for the lower pitch

angles. Given that pressure forces are usually higher than skin friction drag, it is expected that the same result will still apply at higher pitch angles.

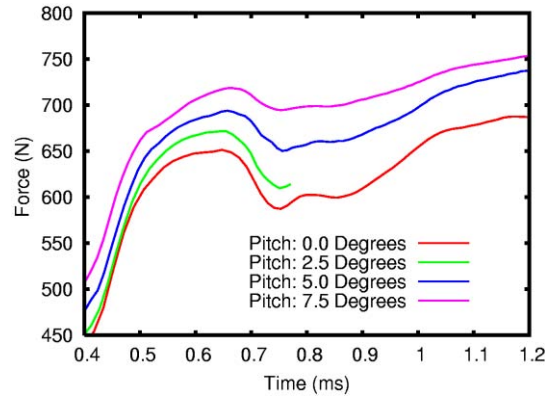


Figure 5. X-Component of aerodynamic force in Newtons exerted on the EFP at all pitch angles.

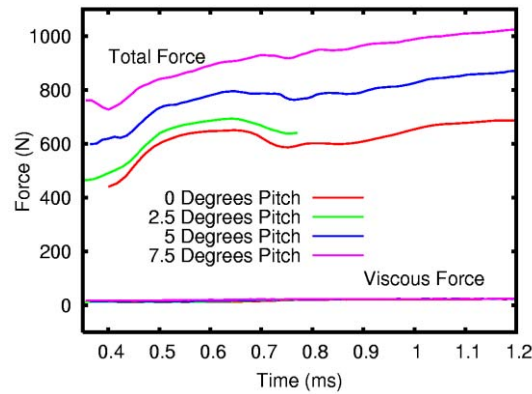


Figure 6. Total force magnitude in Newtons compared with viscous force magnitude for all pitch angles.

B. Turbulent Flow Field Physics

Typical hypersonic flow characteristics are exhibited near the blunt nosed EFP. The proximity of the detached bow shock wave motivates an examination of the flow field around the body. Our hybrid LES simulation easily affords doing so, but it is important to bear in mind the limitations of 3D field post-processing. Recall that the computational grid consists of 243 subdomains; each subdomain consists of one structured grid, but there is no global index system, (i.e., an (i, j, k) ordered triple) available to address the grid on the whole. To accurately extract data from the flow field, we normally plot along constant index planes to obtain a smooth flow field property distribution. For complex domain decompositions, it is not possible to plot data smoothly along such planes. As a result, the post-processor is required to interpolate between constant index planes over more than one subdomain. This deficiency can cause the plotting program to create uneven contours. This difficulty is illustrated in Figures 7 and 8, plots of flow field properties generated at the nose of the EFP. Figure 7 contain plots of gas density and pressure. Although the contours in these figures suffer from gaps due to interpolation, we can clearly see the formation of a bow shock that stands away from the nose. The shock wave is identified as a yellow-red high density region separated from the nose by a blue low density region. Moreover, Figure 7 also shows the high pressure post-shock region very clearly. Figure 8 illustrates the region of high vorticity behind the curved shock, and we can also see subgrid kinetic energy spike in this region. The results conveyed by Figure 8 are very important; they clearly convey the presence of strong turbulent eddies near the EFP body. Both vorticity and subgrid kinetic energy take on a wide range of values at the nose. The resulting strong gradients in these quantities advect along the surface of the EFP. Hence, the EFP boundary layer is turbulent. If turbulence were not generated at the nose, we would see

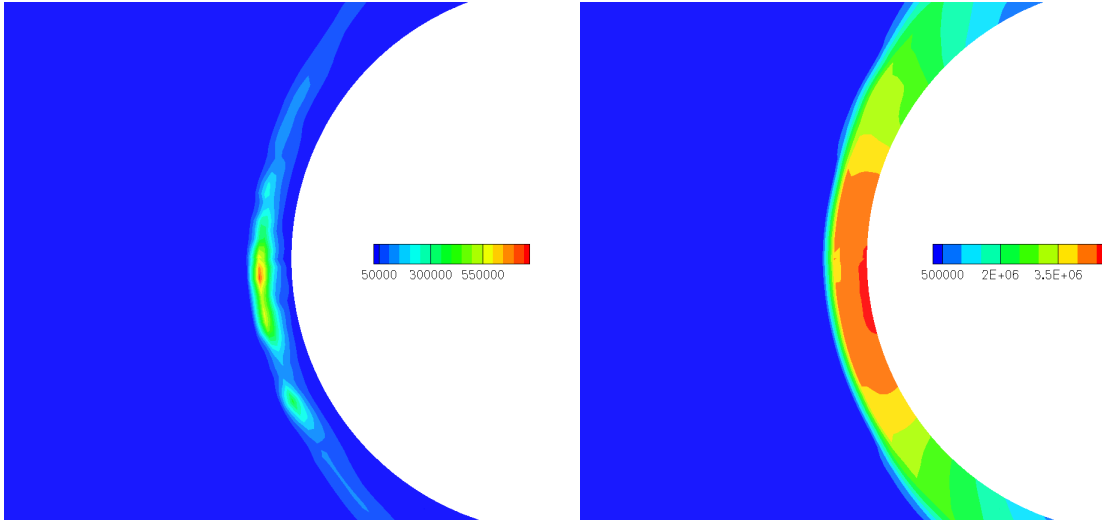


Figure 7. Contours of flow field (left) density in kg/m³ and (right) pressure in Pascals generated along the central z plane at the nose of the EFP. Plots correspond to 1.35 ms of elapsed time for the 5° pitch case.

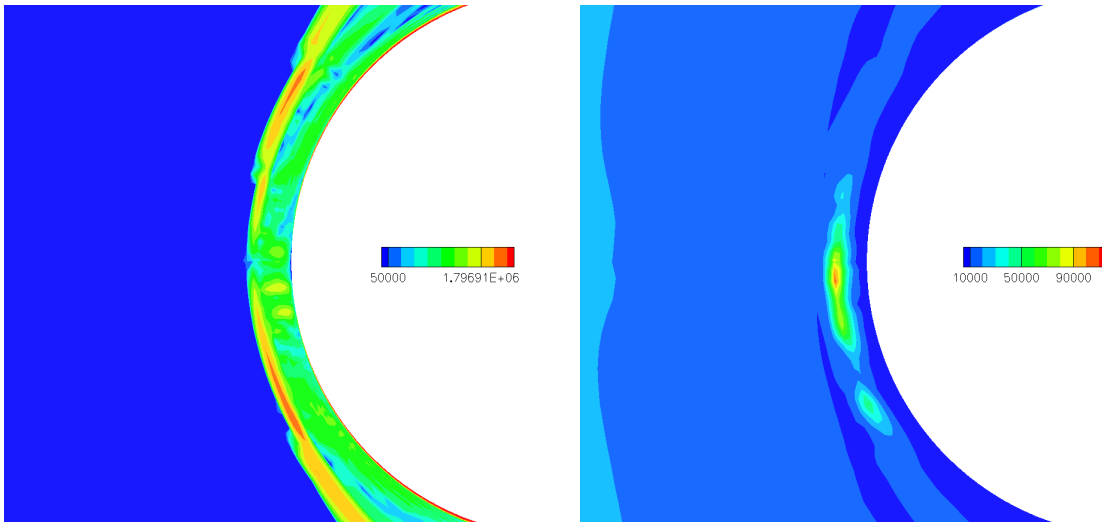


Figure 8. Contours of flow field (left) vorticity in s⁻¹ and (right) subgrid kinetic energy in m²/s² cast along the central z plane at the nose of the EFP. Plots correspond to 1.35 ms of elapsed time for the 5° pitch case.

turbulence die out as the solution progresses. This behavior would be assured by the dissipation term in Equation (14). Figure 8 is especially significant when viewed along with Figures 9 and 10. Figure 9 contains plots of subgrid kinetic energy taken at the first cell adjacent to the external body surface. The first plot is generated along a longitudinal curve starting at the nose of the EFP and terminating at its trailing end. The curve is confined to the xz -plane on the “top” surface of the EFP. The second plot is generated along an azimuthal ring circling the EFP body parallel to the yz -plane at the location $x=3.659$ mm. The existence of turbulence is clearly indicated in Figure 9. The longitude plot shows strong fluctuations in subgrid kinetic energy along the length of the EFP body with the strongest turbulent eddies existing behind the nose and near the “shoulder region” for the EFP. The magnitude of the turbulence varies by as much as a factor of ten. Between the two solutions shown in time, one can see a disturbance in subgrid kinetic energy propagating from the tail toward the nose in the subsonic boundary layer. The azimuth plot (left in Figure 9) shows significant changes in this energy around the body occurring over time.

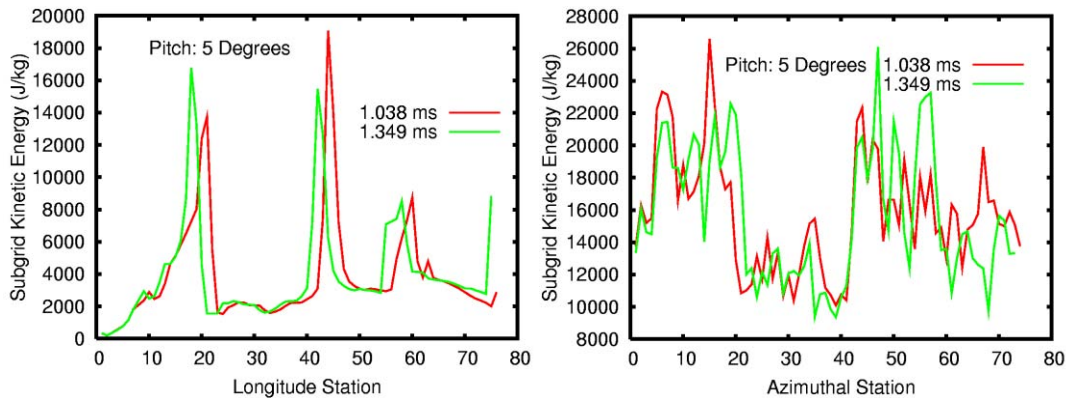


Figure 9. Subgrid kinetic energy (J/kg) calculated in the first cell adjacent to the body: (left) along a longitudinal curve from nose to trailing end, and (right) along an azimuthal ring a short distance behind the nose for the 5° pitch case.

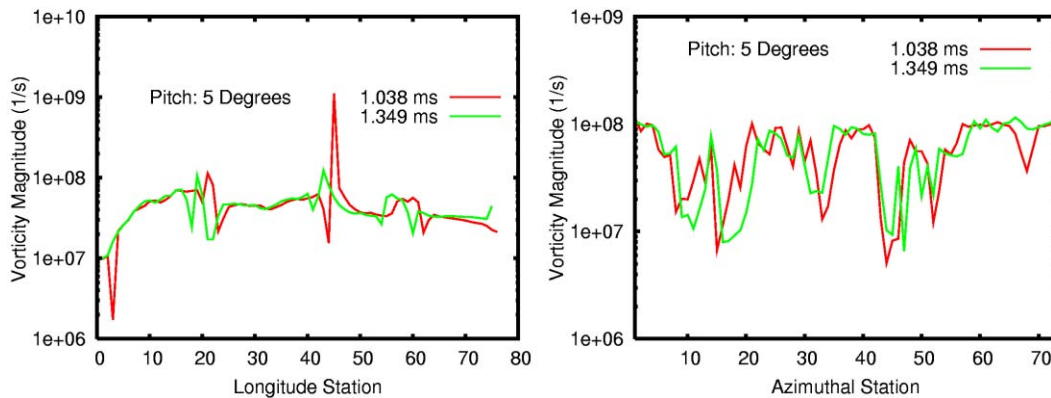


Figure 10. Vorticity magnitude (s^{-1}) calculated in the first cell adjacent to the body: (left) along a longitudinal curve from nose to trailing end, and (right) along an azimuthal ring behind the nose for the 5° pitch case.

Interestingly, the strongest fluctuations occur on the “sides” of the EFP subjected to cross-flow conditions. Based upon the behavior of subgrid kinetic energy in these regions, it is worthwhile to examine the magnitude of vorticity shown in Figure 10. The range of vorticity magnitude is so wide, we have employed a log scale for plotting. Note that the longitude plot also reveals the existence of a disturbance propagating upstream in the boundary layer. Vorticity also spikes in essentially the same locations predicted by Figure 9. The azimuth plot indicates that in time vorticity fluctuates strongly around the body especially in areas with strong fluctuations in subgrid turbulent kinetic energy. By revisiting Figure 8 (left), we observe that bubbles of high vorticity develop in the nose and shoulder regions and then advect along the body surface. This information confirms that a turbulent flow field driven by localized sources exists around the EFP during its flight. Also, vorticity seems to be coupled with gradients in subgrid kinetic energy. For these reasons, it is doubtful that the EFP flow field can attain stationary flow conditions within its short time of flight.

C. The Distribution of Temperature

Hypersonic bluff body flow fields are characterized by the presence of high temperature gas dynamics. Slices of the temperature flow field are presented Figure 11 for the 5° pitch case. The presence of a high temperature bubble is evident at the EFP nose. The temperature in this neighborhood rises above 2000°K; as a result, the gases become hot enough to support limited chemical ionization.³ This assertion is also supported by Figure 8 since the subgrid kinetic energy, a driver for chemical reactivity, becomes very high in this region. The strong

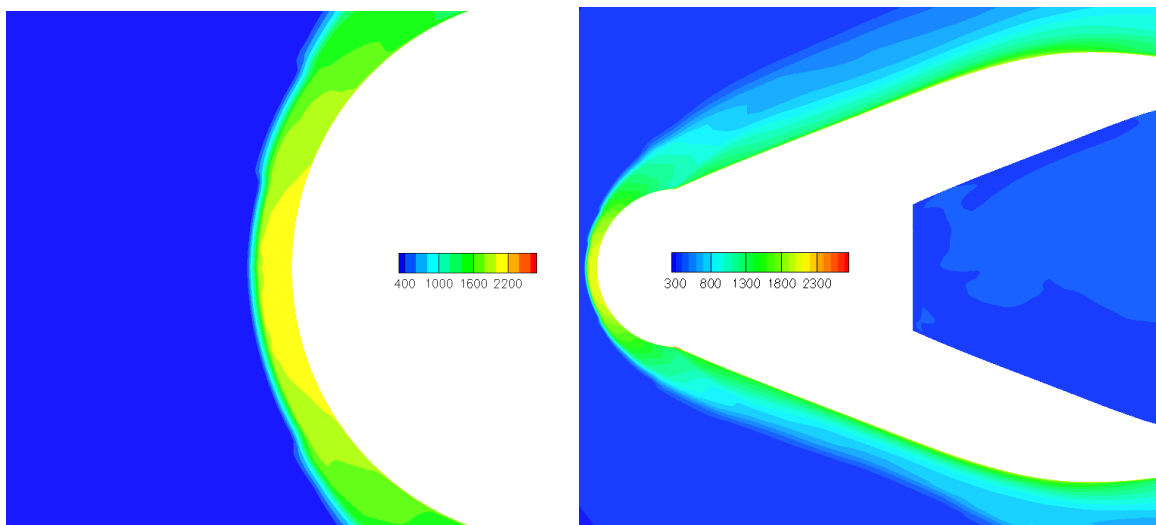


Figure 11. Flow field temperature in Kelvin along the central vertical mid-plane at (left) the nose and (right) for the nose and shoulder region. In the plot on the right, the large blue region is for the interior of the EFP.

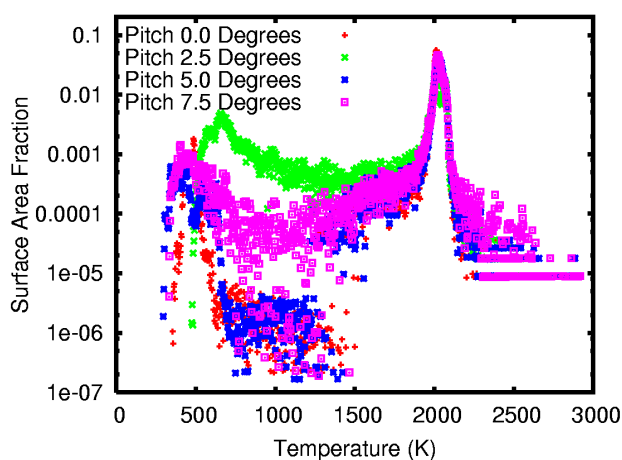


Figure 12. EFP Surface Area Fraction versus surface temperature (K) for all pitch angles.

range, ionization reactions become likely for Oxygen. As a result, this calculation is to be performed with finite rate turbulent chemistry algorithms activated. It is possible that the surface of the EFP may also be wetted by an ion field. If so, the flow properties around the body would be altered. In any case, the higher gas temperatures indicated near the body motivate a detailed examination of temperature along the body surface. An EFP's in-flight survivability is largely a function of its surface temperature since the structural integrity of the EFP depends on thermal softening of the metal liner. If regions of high temperature occur on the body, the EFP may, under aerodynamic loading, break apart in flight. For the 5° pitch case, the external and internal surface temperature plots are shown in Figure 13 at 1.21 ms solution time. Similar behavior is observed at other pitch angles. As one may expect, there are large differences in temperature between the exterior and interior surfaces. It is interesting to see that the high and low temperature spatial distributions nearly reverse between the exterior and interior. This phenomenon is likely to be due to recirculating flow at the base of the EFP. Of course, the interior exists at cooler temperatures than the exterior surface since our model does not capture conductive heat transfer through the metal liner. Still, we can easily calculate temperature gradients on these surfaces. The plots are shown in Figure 14. The

correlation between temperature and subgrid kinetic energy lends to the likelihood of chemical reactions. When time permits, this problem may be solved using turbulent chemistry algorithms since the attendant changes to the flow field can affect EFP motion. It is interesting to analytically examine the distribution of temperature over the body surface at different pitch angles. Figure 12 addresses this subject by dividing the temperature range from 200°K to 3000 °K into bins. We then sum the incremental areas along the EFP surface that are "wetted" by temperature within the respective bins. This Figure illustrates the fraction of EFP surface area subjected to temperatures within the overall range. Although the solution corresponding to the 2.5° pitch angle has not fully matured, Figure 12 reveals useful information. We note that there is a strong concentration of surface area corresponding to the temperature band between 2000°K and 2100°K. In this

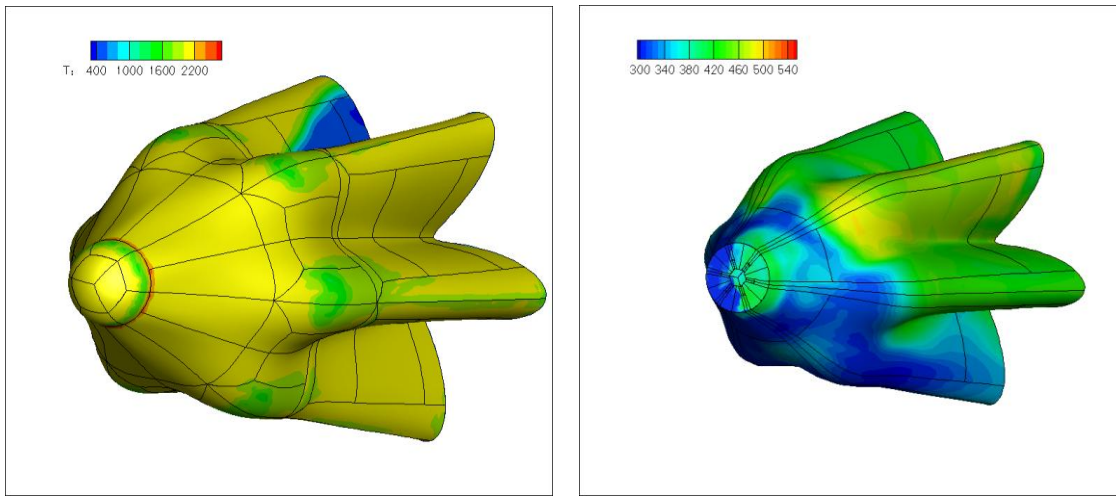


Figure 13. Temperature (K) distributions on the (left) exterior and (right) interior surfaces of the EFP at 5° pitch angle, solution time 1.21 ms.

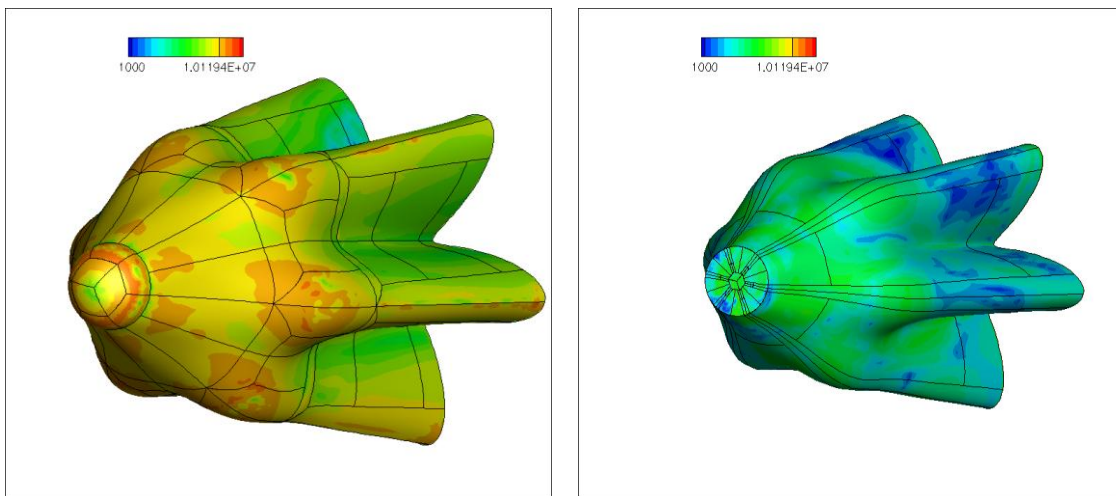


Figure 14. Magnitude of temperature gradient (K/m) distributions on the (left) exterior and (right) interior surfaces of the EFP at 5° pitch angle, solution time 1.21 ms.

magnitude of the temperature gradient on the exterior surface is, to say the very least, intense, particularly near the oblique surfaces of the nose, on the shoulders and on the longitudinal ribs of the EFP. The differential change in the gradient is less pronounced on the interior surface, but the greater part of the EFP body surface is subjected to very high thermal gradients with associated thermal stress. It is also important to realize that any irregularity (or crease) in or on the body results in a region of high temperature due to frictional heating. Note that in Figure 13 there is ring-shaped defect just behind the nose that is subject to temperatures exceeding 2200°K. The fact is important since for real EFPs, body surface irregularities are commonplace. The strong localization of temperature indicated leads one to wonder at how other properties might be distributed over the EFP surface. Consider vorticity magnitude as an example. This property is presented in Figure 15 for the exterior surface. As is indicated by this plot, vorticity changes by over a factor of 10 on the body. Hence, the boundary layer is subject to violent mixing, and the spotty

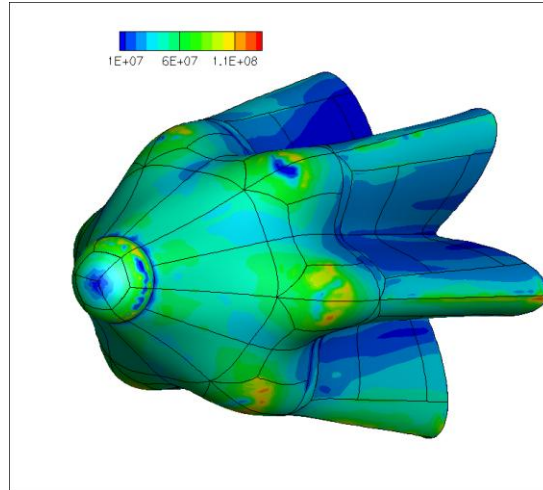


Figure 15. Distribution of vorticity magnitude (s-1) on the exterior EFP surfaces at 5° pitch angle, solution time 1.21 ms.

turbulent fluctuations in vorticity are clearly evident. Strong vorticity fluctuations can affect the pressure distribution at the body surface and impact aerodynamic loading. Hence, predicted EFP motion can be altered by the accuracy of the aerodynamic model. An important conclusion is that, due to this mixing, accurate turbulence models must be used in order to accurately predict the temperature distribution for the EFP in time.

IV. CONCLUSIONS

In the course of this research, we have performed a time-accurate simulation of the time-dependent hypersonic, impulsively started flow field evolving around a generic EFP shape. The example simulation, performed with the use of the LESLIE3D multiphase physics computer code, has been conducted at Mach 6 in a normal atmospheric mixture of Oxygen and Nitrogen under sea level flight conditions for a series of pitch angles. LESLIE3D is a massively parallel computer code capable of the high fidelity resolution of shock-turbulence including chemical reactions. Our goal has been to capture the physics associated with this flow field as accurately as possible by using state-of-the-art LES techniques. The temperature field is resolved with the use of the Thermally Perfect Gas equation of state. A principal conclusion of this research is that the EFP flow field is characterized by the presence of a highly turbulent boundary layer. Effects of this turbulence must be accounted for in the calculation of loads due to the interaction of subgrid kinetic energy with regions of high vorticity. Fluctuating fields of subgrid kinetic energy advect through the boundary layer; upstream feedback is also noted in this region. Unsteady features in the flow field are so prevalent that it is unlikely that flow stationarity is achieved during the EFP's flight time. This issue further complicates issues associated with aerostability. We have also investigated, in some detail, the temperature distribution on the exterior and interior surfaces of the EFP. Purely from the standpoint of aerodynamics, areas of severe temperature gradient and possible thermal shock have been revealed. We have also identified temperature regions in the flow field that may support the existence of ionization reactions that may further impact the dynamics of this system. Given the turbulent nature of the flow field, ionization, a form of chemical reaction, should be investigated. We plan to investigate these effects in future work associated with this project. The present studies are limited to fixed geometric body configurations; however, we plan on implementing new algorithms to incorporate time-dependent deformation of the EFP body in the near future.

Acknowledgments

This work was sponsored by the Air Force Office of Scientific Research.

References

- ¹Vanden, K., Ellison, S. and Wilson, J., “Hypersonic and Unsteady Flow Science Issues for Explosively Formed Penetrator Warheads”, 2nd Revision, Computational Mechanics Branch, Munitions Directorate, Air Force Research Laboratory, 2007.
- ²Hankey, W.L., *Re-Entry Aerodynamics*. AIAA Education Series, American Institute of Aeronautics and Astronautics, Washington, DC, 1988.
- ³Anderson, J.D., Jr., *Hypersonic Flow and High Temperature Gas Dynamics*. MacGraw-Hill, Inc., New York, 1989.
- ⁴Erlebacher, G., Hussaini, M.Y., Speziale, C.G. and Zang, T.A., “Toward the large-eddy simulation of compressible turbulent flows”, *Journal of Fluid Mechanics*, Vol. 238, 1992, pp. 155-185.
- ⁵Menon, S., “Direct and Large-Eddy Simulations of Solid Propellant Combustion and High-Energetic Detonation in Reactive Mixtures”, Annual Report for Grant N00014-01-1-0951, Office of Naval Research, 2007.
- ⁶Sankaran, V. and Menon, S., “LES of spray combustion in swirling flows”, *Journal of Turbulence*, Vol. 3, No. 1, 11, 2002.
- ⁷Génin, F., Fryxell, B. and Menon, S., “Simulation of Detonation Propagation in Turbulent Gas-Solid Reactive Mixtures”, *41st AIAA/ASME/SAE/ASEE Joint Propulsion Conference & Exhibit*, Tucson, Arizona, 2005.
- ⁸Génin, F. and Menon, S., “Simulation of Turbulent Mixing Behind a Strut Injector in Supersonic Flow”, *47th AIAA Aerospace Sciences Meeting*, Orlando, Florida, 2009.
- ⁹Ukai, S., Génin, F., Srinivasan, S. and Menon, S., “Large Eddy Simulation of Re-shocked Richtmyer-Meshkov Instability”, *47th AIAA Aerospace Sciences Meeting*, Orlando, Florida, 2009.
- ¹⁰Gottiparthi, K.C., Génin, F., Srinivasan, S. and Menon, S., “Simulation of Cellular Detonation Structures in Ethylene-Oxygen Mixtures”, *47th AIAA Aerospace Sciences Meeting*, Orlando, Florida, 2009.
- ¹¹Toro, E.F., *Riemann Solvers and Numerical Methods for Fluid Dynamics – A Practical Introduction*. Addison-Wesley Publishing, Co., Inc., 1999.
- ¹²Einfeldt, B., Munz, C.D., Roe, P.L. and Sjogreen, B., “On Godunov-type methods near low densities”, *Journal of Computational Physics*, Vol. 92, 1991, pp. 273-295.
- ¹³Génin, F., “Study of Compressible Turbulent Flows in Supersonic Environment by Large Eddy Simulation”, Ph.D. Dissertation, School of Aerospace Engineering, Georgia Institute of Technology, Atlanta, Georgia, May 2009.
- ¹⁴Hirsch, C., *Numerical Computation of Internal and External Flow, Volume 2*. John Wiley & Sons, Inc., New York, 1991.
- ¹⁵Collela, P. and Woodward, P., “The piecewise-parabolic method for hydrodynamics”, *Journal of Computational Physics*, Vol. 54, 1984, pp. 174-201.
- ¹⁶Fryxell, B. and Menon, S., “Hybrid Simulations of Richtmyer-Meshkov Instability”, *43rd Aerospace Sciences Meeting and Exhibit*, Reno, Nevada, January 2005.